Bulletin of the Seismological Society of America, Vol. 79, No. 2, pp. 500–514, April 1989

WAVEFORM MODELING OF THE NOVEMBER 1987 SUPERSTITION HILLS EARTHQUAKES

BY ALLISON L. BENT, DONALD V. HELMBERGER, RICHARD J. STEAD, AND PHYLLIS HO-LIU

ABSTRACT

Long-period body-wave data recorded at teleseismic distances and strong-motion data at Pasadena for the Superstition Hills earthquakes of 24 November 1987 are modeled to obtain the source parameters. We will refer to the event that occurred at 0153 UT as EQ1 and the event at 1316 UT as EQ2. At all distances the first earthquake appears to be a simple left-lateral strike-slip event on a fault striking NE. It is a relatively deep event with a source depth of 10 km. It has a teleseismic moment of 2.7×10^{25} dyne cm. The second and more complex event was modeled in two ways: by using EQ1 as the Green's function and by using a more traditional forward modeling technique to create synthetic seismograms. The first method indicated that EQ2 was a double event with both subevents similar, but not identical to EQ1 and separated by about 7.5 sec. From the synthetic seismogram study we obtained a strike of 305° for the first subevent and 320° for the second. Both have dips of 80° and rakes of 175°. The first subevent has a moment of 3.6×10^{25} which is half that of the second. We obtain depths of at least 6 km. The teleseismic data indicate a preferred subevent separation of 30 km with the second almost due south of the first, but the error bounds are substantial. This would suggest that the subevents occurred on conjugate faults. The strong-motion data at PAS, however, imply a much smaller source separation, with the sources probably produced by asperities.

INTRODUCTION

The Superstition Hills earthquakes of 24 November 1987, hereafter referred to as EQ1 (at 0153 UT) and EQ2 (at 1316 UT) occurred near the edge of a complex basin that has produced many moderate to large earthquakes in the past (1968 Borrego Mountain, 1969 Coyote Mountain, 1979 Imperial Valley, 1981 Westmorland). Field investigations and aftershock patterns (Fig. 1) indicate that EQ1, which occurred a few kilometers SW of the southern end of the Salton Sea, occurred on a previously unknown NE-striking left-lateral fault. EQ2 occurred 10 km SW of EQ1 and ruptured the right-lateral Superstition Hills fault, which is roughly perpendicular to the fault that produced EQ1. The epicenter of EQ2 is located at or near the junction of the two faults. The aftershocks of EQ2 line up roughly parallel to the Superstition Hills fault but are located between the Superstition Hills and Superstition Mountain faults (Fig. 1).

DATA

Both November events as well as a smaller (M_L 4.9) aftershock that occurred on 28 January 1988 (EQ3) were well recorded at Pasadena (PAS), about 250 km to the NW (Figs. 2 and 3). Because EQ3 was a small event, it was recorded on scale by more Caltech stations at local distances (<200 km) than were EQ1 and EQ2, so its depth and focal mechanism are well determined from local data. EQ3 can be well modeled at PAS using regional Green's functions for the path from Imperial Valley to Pasadena obtained by modeling regional Love waves for a large number of past

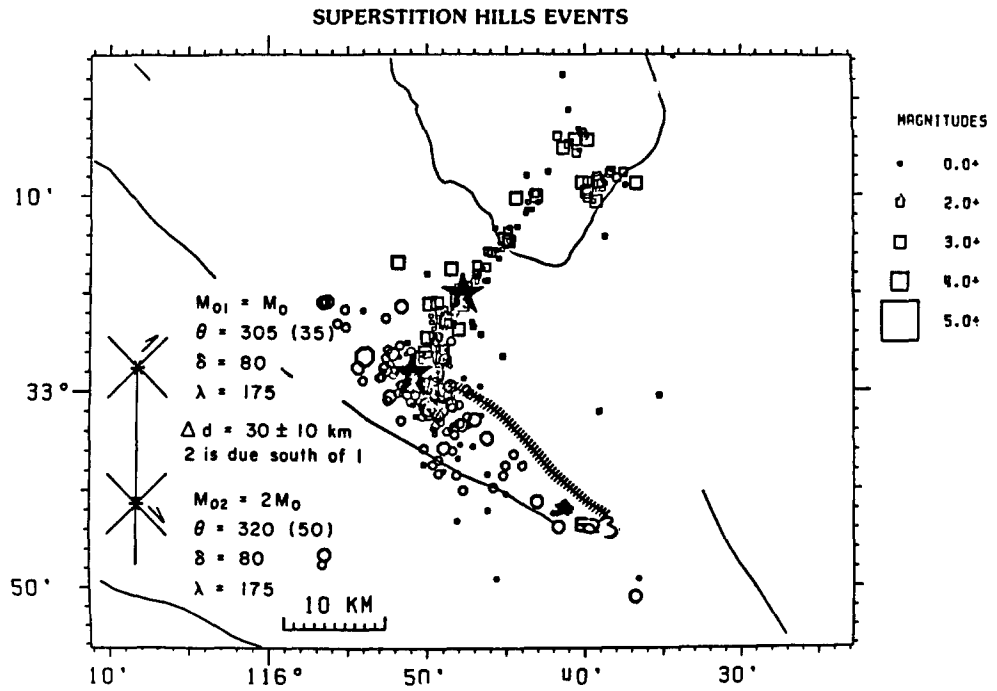

FIG. 1. Locations of Superstition Hills events (modified from Magistrale *et al.*, 1989). The squares represent events occurring before EQ2 and the circles are events occuring after EQ2. The large stars are EQ1 and EQ2 (EQ2 is SW of EQ1). The hatched line shows the extent of rupture on the Superstition Hills fault. In the lower left-hand corner, the approximate relative locations of the 2 subevents of EQ2 are shown. The arrows represent the probable direction of rupture based on strong-motion data (Wald and Somerville, 1988).

events in the Imperial Valley region (Ho-Liu and Helmberger, 1989). In this way we can use EQ3 to help constrain the faulting parameters of EQ1 and EQ2.

At PAS EQ1 and EQ2 were recorded by a short-period low-gain (100×) Wood-Anderson instrument and EQ3 was recorded by our newly installed broadband (bb) instrument, so before we can compare them we have to give them the same instrumental response (Fig. 3). The top trace of Figure 3 displays the bb displacements for EQ3 and is followed by rows of simulated responses appropriate for the various PAS conventional instruments. The numbers indicate the predicted peak amplitudes in cm with the instrumental gains included. Hand digitized and rotated Press-Ewing responses (30, 90) yield nearly identical records to the bb instrument with nearly the same absolute amplitudes. That is the observed peak tangential motion is 2.5 cm compared to 2.4 cm, and so on. The observed 30, 90 tangential motion agrees well with that of similar magnitude Brawley events and can be modeled (Ho-Liu and Helmberger, 1989). Unfortunately, the long-period recordings of EQ1 and EQ2 are off-scale.

In many situations, an aftershock recorded on a long-period Wood-Anderson instrument (gain = 1700) looks very similar to the main event recorded on a short-period Wood-Anderson instrument (gain = 100). Presumably, the shift in corner frequency is off-set by the instrumental response and the difference in strength is handled by the gain differential (Ho-Liu and Helmberger, 1989). Such a comparison is given in Figure 4 along with a theoretical response. The depth phase *sS* appears clear for both events and indicates a depth of 10 km for both.

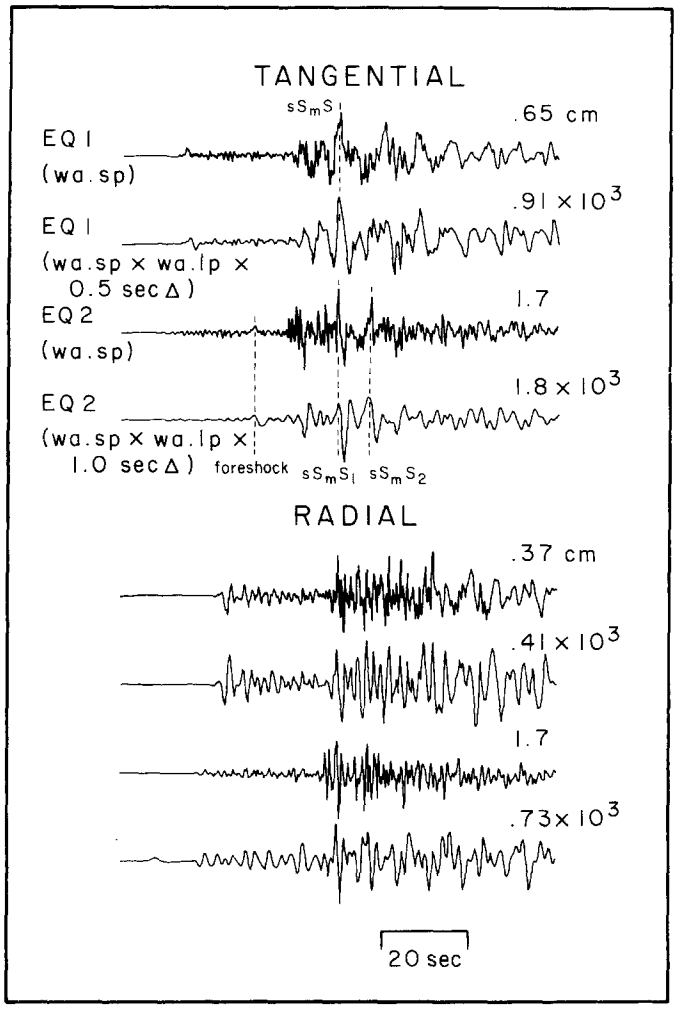

FIG. 2. Tangential and radial data for EQ1 and EQ2 recorded at PAS. The upper trace is EQ1 raw data (recorded on a short-period Wood-Anderson instrument); the second trace is the EQ1 data convolved with a long-period Wood-Anderson instrument and a 0.5-sec triangle filter; the third is the EQ2 data; the fourth is EQ2 convolved with a long-period Wood-Anderson instrument and a 1-sec triangle.

EQ2 is a more complex event than either EQ1 or EQ3 and consists of two or more subevents. If we line up the strong *S* motion at PAS for EQ1 and EQ2 (Fig. 2), we see that EQ2 begins earlier than expected, indicating that it was preceded by a small foreshock. This foreshock was also identified, but treated as an additional subevent by Frankel and Wennerberg (1988, 1989). Because of the foreshock, EQ2 may not be as well located as EQ1 since the network location reflects the foreshock location and not necessarily the location of the main energy release. Such a difference between the epicenter and area of maximum dislocation was seen in the 1979 Imperial Valley earthquake. Although the earthquake was located 5 km south of the California-Mexico border, the maximum dislocation occurred in two localized areas 7.5 and 25 km north of the epicenter (Hartzell and Helmberger, 1982). In Figure 2 it can be seen that EQ2 has smaller surface waves than EQ1 even though EQ1 is a smaller event, indicating that the focal depth of EQ2 is at least as great as that of EQ1 (10.5) km and possibly greater. Since EQ2 was originally located at a

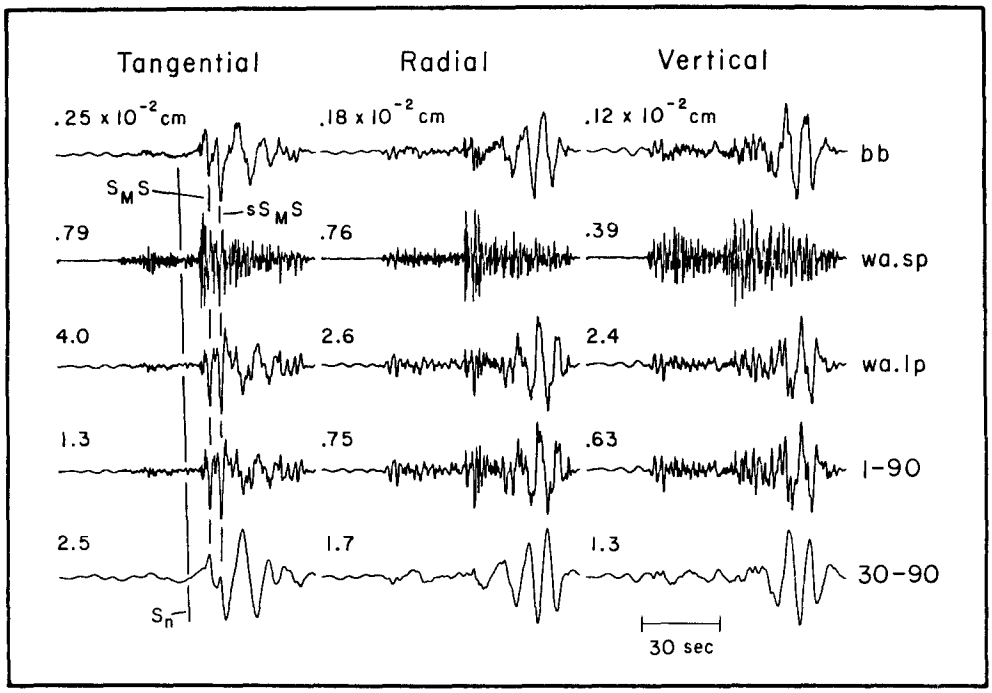

FIG. 3. Tangential (*left*), radial (*middle*) and vertical (*right*) components of EQ3 convolved with various instrument responses. Wa.sp is short-period Wood-Anderson; wa.lp is long-period Wood-Anderson; lp3090 is Press-Ewing.

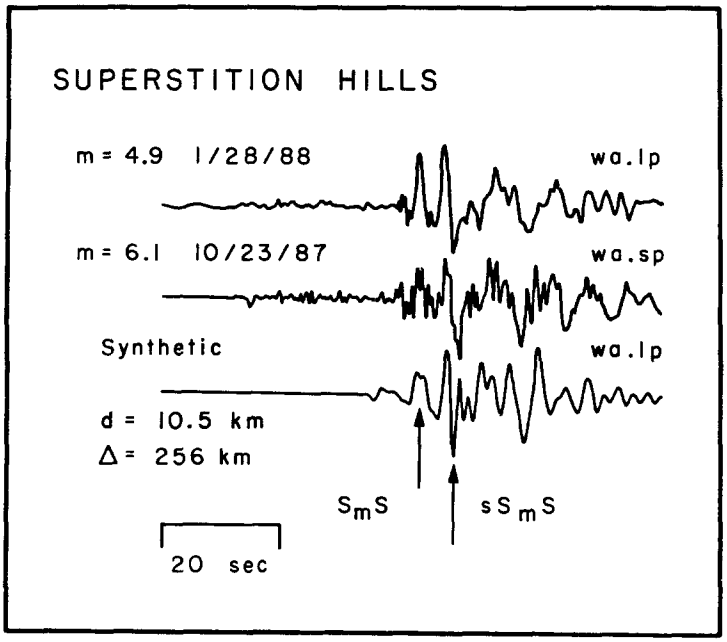

FIG. 4. EQ1 and EQ3 at PAS (tangential component). The lower trace is the synthetic seismogram for EQ3, but it also fits the EQ1 data.

depth of about 2 km (Magistrale *et al.*, 1989), this suggests that indeed there is some discrepancy between the network depth and the actual depth of EQ2. In modeling the teleseismic waves of EQ2 (which will be discussed in a later section), we obtain the best results when we use a depth of 10 km or greater.

Both EQ1 and EQ2 were well recorded teleseismically by the Canadian and GDSN networks. The long-period teleseismic data show that EQ2 is more complex than EQ1 as did the local and regional strong-motion data. The teleseismic records indicate that EQ2 may consist of two subevents similar to EQ1, but with the second subevent larger than the first. Figure 5 shows the raw data for EQ1 and EQ2 as well as the 1968 Borrego Mountain earthquake recorded at STJ. EQ1 and Borrego Mountain appear very similar while EQ2 is more complex. We attempted to reproduce EQ2 by adding EQ1 to itself with a time delay and allowing the size of the second subevent to vary relative to the first. By using a 9-sec delay and making the second subevent twice as large as the first, we are able to reproduce EQ2 from

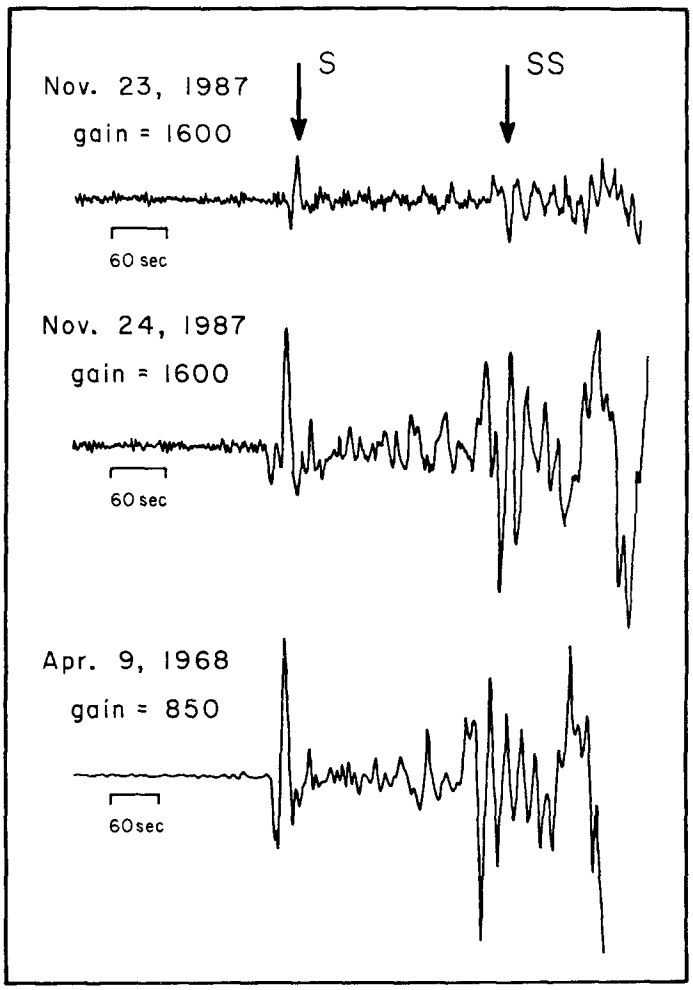

FIG. 5. *SH* data recorded at STJ for EQ1, EQ2 and the 1968 Borrego Mountain event. The data are plotted at the correct relative amplitudes of the original records. Note that the magnification has changed since 1968.

both the EQ1 and Borrego Mountain data (Fig. 6). In modeling EQ2, we use the results of mapping the EQ1 data into EQ2 to obtain the general characteristics of EQ2 and then use these results as a starting point in forward modeling EQ2.

Studies of the strong-motion data (Wald and Sommerville, 1988; Frankel and Wennerberg, 1989) found that the relative size of EQ2's two subevents was a function of azimuth, which was interpreted to be a directivity effect. Wald and Sommerville (1988) concluded that the initial rupture was toward the northeast. There was then a pause in the activity after which the rupture continued, but to the southeast along the Superstition Hills fault. Frankel and Wennerberg (1989) also explored this hypothesis but prefer super-shear rupture along the Superstition Hills fault as the explanation for the observed strong-motion records. We investigate the possibility of rupture on conjugate faults by studying the available teleseismic data, and although the results are inconclusive due to the uncertainties in the relative timing of the two subevents at some stations, our best results indicate that the second subevent occurred due south of the first. In light of the aftershock

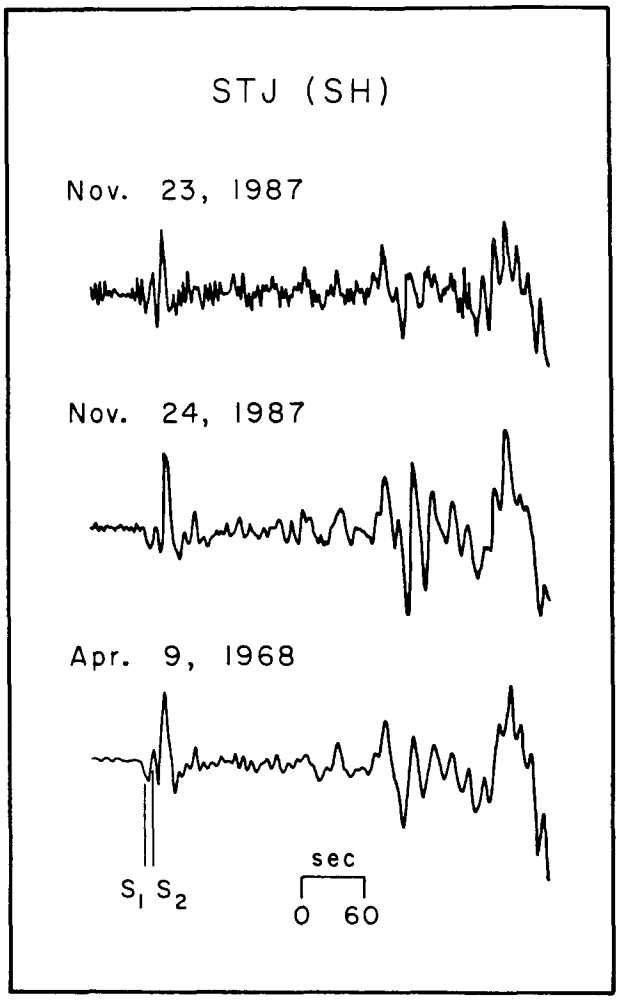

FIG. 6. The middle trace is the *SH* data at STJ for EQ2. The upper trace is the data for EQ1 added to itself with a 9 sec delay and with the delayed event being twice as large as the first. The lower trace is the data for the Borrego Mountain earthquake added to itself with a 9 sec delay. Amplitudes are normalized so that the maximum *S* amplitude is the same on all three traces.

distribution and known fault geometry, the most reasonable locations for the two events separated in this manner would be to place the first subevent on the same fault as EQ1 and the second subevent on the Superstition Hills fault.

A study of slip associated with these earthquakes (Williams and Magistrale, 1989) showed that about 75 per cent of the slip was postseismic, and that the amount of postseismic slip was higher at the southern end of the aftershock zone along the Superstition Hills fault. Co-seismic surface rupture was also inferred at the southern end of the Superstition Hills fault. Williams and Magistrale (1989) interpreted this effect to be due to the thicker sediment at the southern end of the fault. Whatever the reason, it appears that much of the long-period energy release occurred on the southern segment of the fault. Long-period teleseismic modeling requires a large spatial separation of the two subevents and locates the second subevent at the southern end of the aftershock zone. Co-seismic surface rupture was also observed at the southern end of the Superstition Hills fault. The observed postseismic creep is compatible with the source separation obtained by modeling.

Teleseismic Modeling

We employed the forward teleseismic modeling technique of Langston and Helmberger (1975) where contributions of various ray paths, including depth phases, are summed. The basin structure was simplified to 2 layers over a half-space (Table 1). The upper layer is a 3 km thick low-velocity layer with velocities that are a weighted average of the near surface layers of the Fuis *et al.* (1982) model for the Imperial Valley. The lower layer is a "normal" crustal layer 12 km thick. The half-space has upper-mantle velocities. Since these events occurred at the edge of the basin, there is some concern about the adequacy of assuming a laterally homogeneous velocity model (Magistrale et al., 1989). Basin edge effects will be addressed in a subsequent study.

EQ1

The results for EQ1 are displayed in Figures 7 and 8. We have included a P_{nl} waveform (regional) to expand the data coverage. The details of modeling regional phases are discussed in Wallace and Helmberger (1982). In general the synthetics fit the data well. At some eastern Canadian stations however, the initial *SH* arrival is noticeably larger than the observed first arrival. This occurs only at analog stations. Changing the focal mechanism does not improve the fit of this phase. The problem is probably the result of trade-offs in the source time function, frequency, and crustal velocity structure. The digital stations have longer period instruments than the analog stations and are therefore less sensitive to small changes in the duration. When we used a half-space model, the initial *S* arrivals were not abnormally large, but the *P* synthetics did not fit the data, so we used a more realistic velocity model. With the basin velocity structure and a longer time function (5 to 6 sec duration instead of 1 to 2 sec), the problem of the large first arrival can be

TABLE 1
Velocity Model

P-Wave Velocity (km/sec)	*S*-Wave Velocity (km/sec)	Density (g/cm^3)	Thickness (km)
3.7	1.4	1.6	3
6.2	3.5	2.7	13
7.9	4.6	3.4	

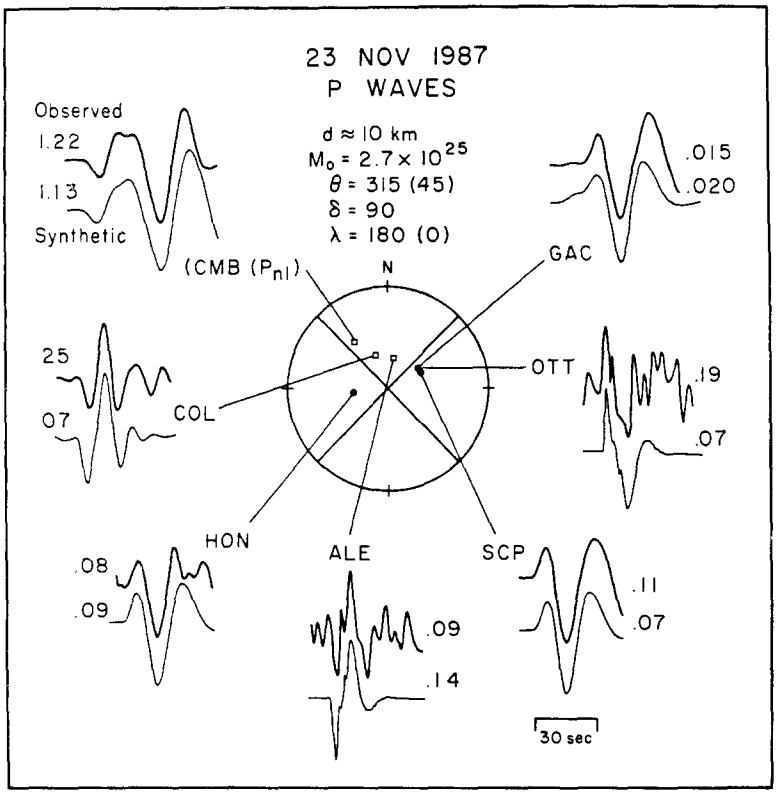

FIG. 7. *P*-wave data and synthetics for the best-fitting EQ1 solution. The upper trace is the observed waveform; the lower is the synthetic. Amplitudes are given in units of 10^{-3} cm and the instrument gain has been removed from the observed waves.

partially alleviated, but the overall frequency content of the synthetics does not fit the data. We use a short time function, because it produces the observed frequencies at all stations and the observed relative amplitudes at most stations. An exact time function has not been determined, because the long-period waves are not sensitive to small changes in the time function, but a triangle of 1 to 2 sec duration produces generally good results.

In short, the long-period modeling of EQ1 confirms that it is a simple deep event, at roughly 10 km. The best fitting focal mechanism is a vertical pure strike-slip fault striking 315° or 45°. Based on the observed surface rupture and aftershock pattern (Magistrale *et al.*, 1989) the left-lateral or NE-striking plane is probably the fault plane. The moment determined from *SH* modeling is 2.7×10^{25} dyne cm, which is in good agreement with the P_{nl} moment of 2.9×10^{25}. The teleseismic *P* waves, however, fit best with a slightly higher moment (3.3×10^{25}).

EQ2

The raw data show that EQ2 is more complex than EQ1 and consists of two subevents each similar to EQ1 as discussed earlier. We can reproduce the EQ1 data by adding the EQ2 data to itself (Figs. 9 and 10), but the relative moments of the first and second subevents change with azimuth, suggesting that the strikes of the two subevents are not identical. The time separation between the two subevents appears to be a function of both azimuth and phase, which suggests that the subevents are separated spatially. We tried a large number of solutions, some with

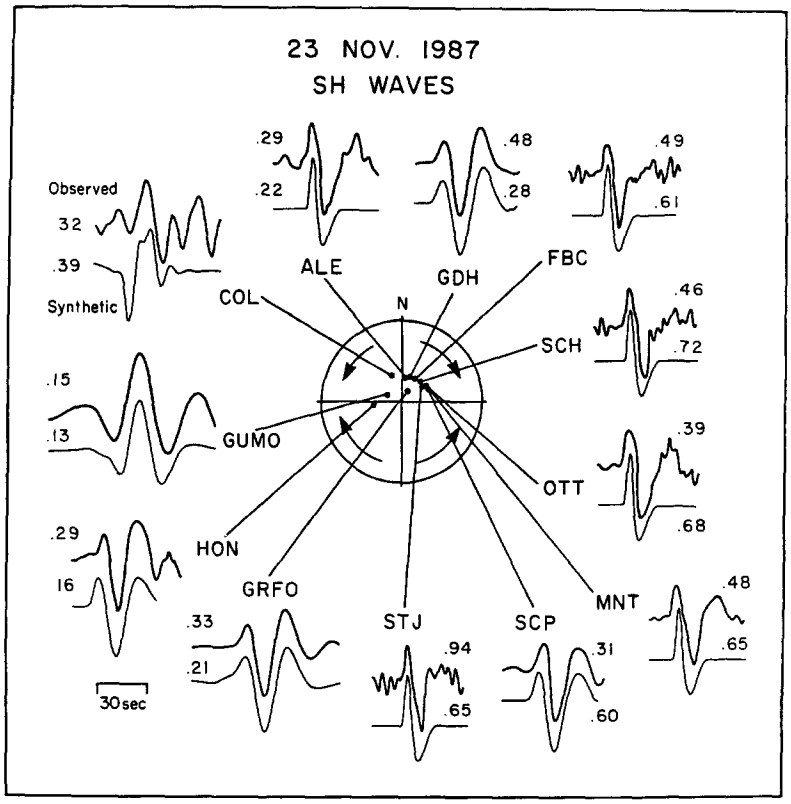

FIG. 8. *SH* data and synthetics for EQ1. The format is the same as for Figure 7.

identical focal mechanisms for both subevents and some with different focal mechanisms. The best synthetics were obtained when the first subevent has a strike of 305° and the strike of the second is 320° (Figs. 11 and 12). The best results were obtained for a slightly less than vertical fault with a preferred dip and rake of 80° and 175°, respectively, for each of the subevents. With the above solution, the second subevent has a moment twice as large as the first at all azimuths. We obtain a moment of 3.9×10^{25} dyne cm for the first subevent and 7.9×10^{25} dyne cm for the second. As was noted in the EQ1 synthetics, the initial *SH* arrival at some eastern Canadian stations is larger than the observed arrival. Again the amplitude cannot be corrected by changing the focal mechanism or depth. When we calculate the moment of EQ2 by using the synthetically determined moment for EQ1 and comparing the maximum amplitudes at all stations which recorded both events, we obtain moments of 3.6×10^{25} and 7.2×10^{25} dyne cm for the two subevents.

EQ2 was originally located at a depth of about 2 km (Magistrale *et al.*, 1989). As mentioned previously, our data suggests that this is the location of a small foreshock (or small subevent) and that the bulk of the energy release occurred at a greater depth. The teleseismic data are best modeled when the first subevent has a minimum depth of 10 km and the second has a depth of 6 km or more. Equally good synthetics can be produced with focal depths of up to 15 km for both subevents, but the data do not require depths this great. Very shallow depths produce unsatisfactory synthetic results.

By using the differences in *P* and *SH* delays for the second subevent at stations of different azimuths, we can obtain the spatial and temporal differences between

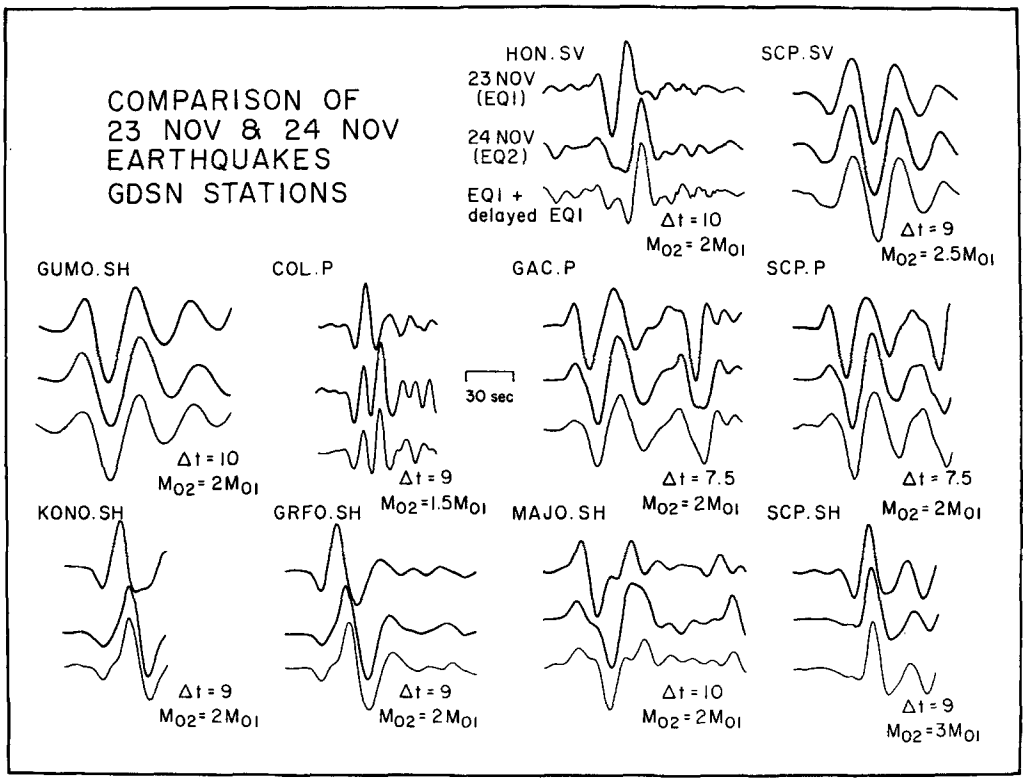

FIG. 9. The upper trace is EQ1, the middle is EQ2 and the lower is EQ1 added to itself with the delays and relative moments as indicated. Amplitudes are normalized to the maximum peak to peak amplitude. The *P* data at HON is clipped and therefore not shown.

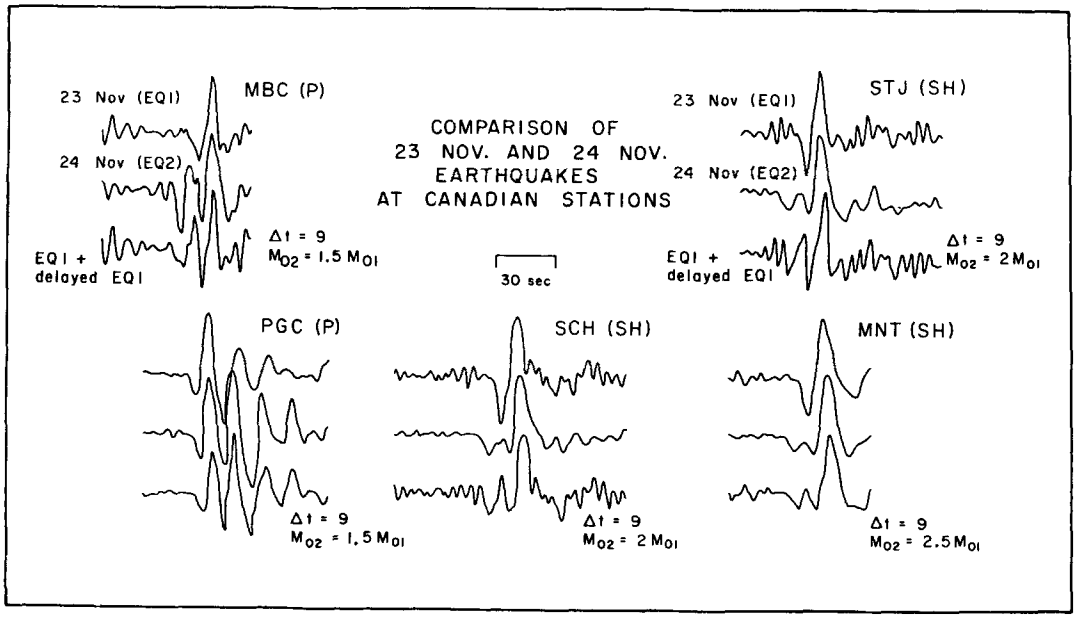

FIG. 10. Canadian data for EQ1 and EQ2. The format is the same as Figure 9.

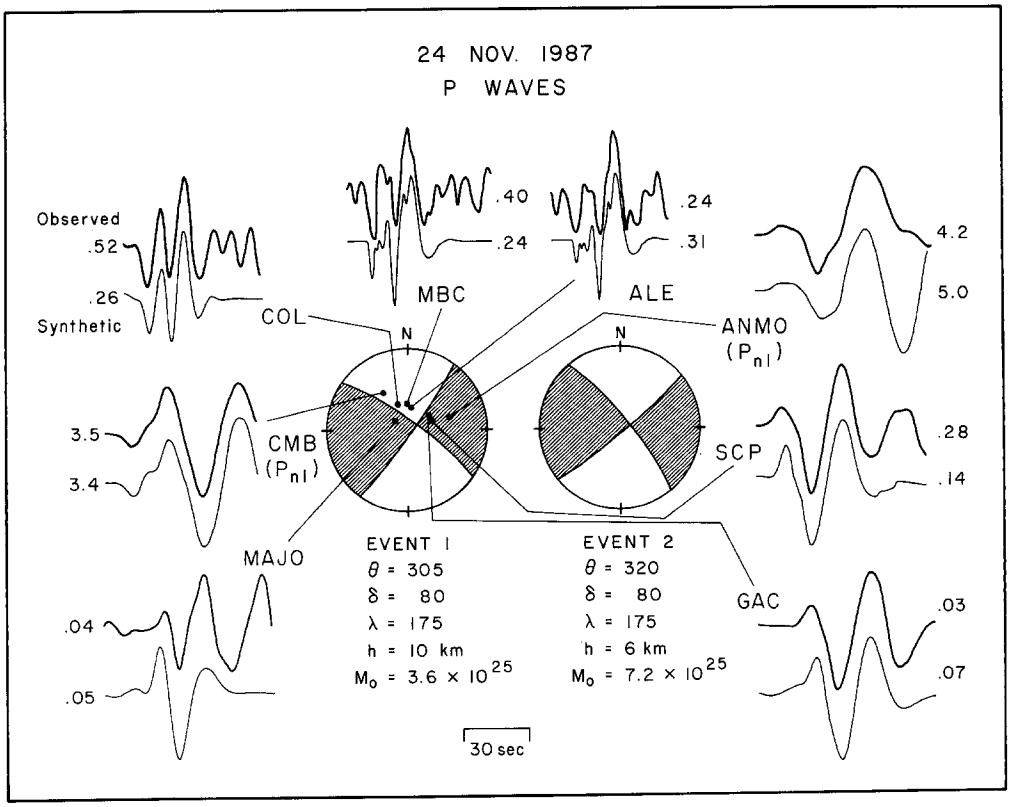

FIG. 11. *P* wave data and synthetics for the best-fitting EQ2 solution. Stations ANMO and CMB are at regional distances; all other stations are at teleseismic distances. The format is the same as that of Figure 7.

the two subevents. Since we have good *P* and *SH* data at SCP, COL, and MAJO, but only one good record at most other stations, we concentrate on these three stations. At SCP we have a 7.5-sec delay between the *P* waves of the two subevents and 9 sec between the *SH* waves. At COL the delays are 9 and 11 sec for *P* and *SH* waves, respectively, and at MAJO they are 9 and 10 sec. We have several eastern Canadian stations with good *SH* waves (SCH, GAC, MNT and STJ), all of which exhibit the 9-sec delay seen at SCP. Northern and western Canadian stations with good *P*-wave data (PGC and MBC) confirm the 9-sec *P* delay observed at COL. The *SH* delay at HON is the same as that at MAJO. The *P* delays at SCP and MAJO and the *SH* delay at COL are probably accurate only to within ±1 sec since the long-period digital data are sampled at a rate of 1 sample/sec and we have no other data at similar azimuths to confirm these delays. Using our best estimates of the delays ($\Delta t_S - \Delta t_P$) and the Jeffreys-Bullen (1940) travel-time tables, we determine the path difference to each station for the two subevents. The azimuth is obtained by determining the location which could produce the observed path differences at all three stations. We calculate that the second subevent occurred 30 km almost due south of the first. Using the minimum *S-P* times at all stations, we obtain a source separation of 8 km with the second subevent SW of the first. A source separation of 50 km is also within the uncertainty of the data, and with a large separation the relative azimuth varies from 125° to 250°. For the average *S-P* times we obtain a time separation of 6.5 sec.

We can also consider P and S waves separately, using Δt_P and Δt_S instead of $\Delta t_S - \Delta t_P$, and the equation (Ben-Menahem *et al.*, 1965)

$$\Delta t = T_0 - D \cos(\phi_o - \phi)P,$$

where Δt is the observed time difference between the subevents at a station, T_0 is the actual time difference between the subevents, D is the spatial separation of the subevents, ϕ_o is the azimuthal separation of the subevents, ϕ is the station azimuth, and P is the ray parameter. The station parameters are summarized in Table 2. For SH waves, we calculate $D = 30.5$ km, $\phi_o = 177°$ and $T_0 = 7.6$ sec. For P waves we obtain $D = 16.2$ km, $\phi_o = 143.5°$, and $T_0 = 7.7$ sec. If we include the uncertainty in Δt at some stations, we obtain a source separation uncertainty similar to that described for the first method.

The local strong-motion data (Wald and Somerville, 1988; Frankel and Wennerberg, 1988, 1989) and the size of the aftershock zone (Fig. 1) are more compatible with a small source separation, but since some of the co-seismic slip and most of

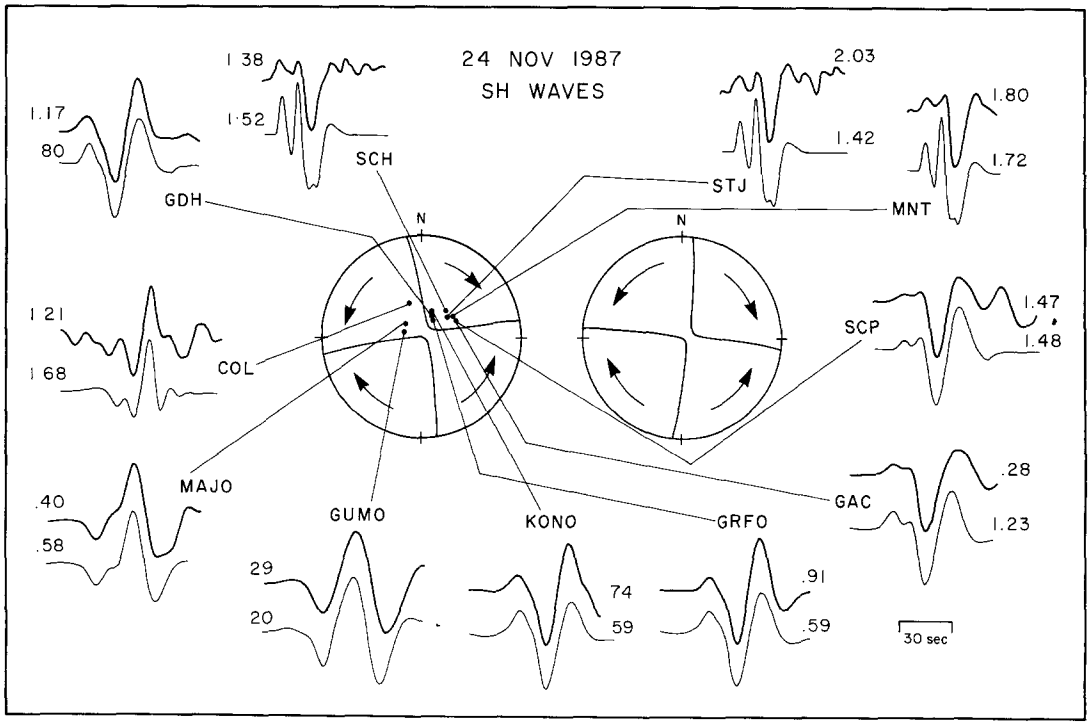

FIG. 12. *SH*-wave data and synthetics for EQ2. All stations are at teleseismic distances. For format, see Figure 7

TABLE 2

STATION PARAMETERS

Station	Δt_p (sec)	Δt_s (sec)	ϕ (deg)
SCP	7.5 ± 1	9	64.5
COL	9	11 ± 1	338.2
MAJO	9 ± 1	10	308.7

the postseismic slip has occurred at the southern end of the aftershock zone, a 30 km separation may not be unreasonable. The apparent discrepancy in source separation may be due to different frequencies of seismic energy being preferentially produced on different segments of the fault. The high-frequency strong-motion energy may be produced by a small high stress drop segment at the northern end of the fault, while the longer period energy can be produced by both high and low stress drop segments.

Differences in the relative amplitudes of the two subevents at local strong-motion stations have been used to infer that the first subevent occurred on the NE-striking plane and the second occurred 7.5 sec later, rupturing toward the south on the NW-striking plane (Wald and Somerville, personal comm.). We tested this hypothesis at teleseismic distances. The 30 km north-south source separation determined from $\Delta t_S - \Delta t_P$, and Δt_S is compatible with the two subevents occurring on conjugate fault planes, but given the large uncertainty in the source separation conjugate faults are not required. The source separation determined from Δt_P, on the other hand, is compatible with both subevents occurring on the Superstition Hills fault and with the Frankel and Wennerberg (1989) interpretation of the strong-motion data. To determine whether the second subevent was a point source or a continuous southward rupture, we distributed the second subevent into a number of smaller but identical events with a total moment the same as that of the point source solution for the second subevent. The relative timing of these smaller events was such that an event located at the same place as the first subevent had a delay equal to the absolute source time separation (7 ± 0.5 sec) and an event 30 km from subevent 1 had a source time separation equal to what was observed at each station. By interpolation and extrapolation, the delays were determined for events at 5 km intervals to a maximum distance of 50 km. The results at most stations were not significantly different from the point source solution, suggesting that whether subevent 2 is a point source or continuous rupture cannot be resolved teleseismically, at least at long periods.

Discussion and Conclusions

As was noted earlier, EQ1 and EQ3 are very similar at PAS, while EQ2 is a more complex event. We attempted to reproduce EQ2 by adding EQ1 and EQ3 to themselves (Fig. 13) with a time delay, in the same manner we reproduced EQ2 from the EQ1 and Borrego Mountain data teleseismically. Since the frequency content of EQ2 is higher than EQ1, we attempted to equalize the frequencies by convolving all seismograms with a long period Wood-Anderson instrument as displayed in Figure 2. Delays from 6 to 10 sec in intervals of 0.5 sec were tested. The best time separation is 8 sec although 7.5 and 8.5 sec produce many features that match EQ2. EQ2 is more similar to two EQ3s than two EQ1s, especially with respect to surface waves. EQ3 occurred at the southern end of the Superstition Hills fault (Fig. 1), where we believe the second subevent of EQ2 also occurred, while EQ1 took place on a perpendicular fault, so it is not surprising that the EQ3 data more closely resemble the EQ2 data than do the EQ1 data. The strong pulses in the synthetics indicated by the dotted lines in Figure 13 are actually associated with *sS* of the two subevents as discussed earlier.

We modeled the second subevent as both a point source and as a continuous source as we did for the teleseismic waves. The point source model produced better results than did the continuous source model, which resulted in surface waves much larger than those observed. We were not able to eliminate the surface waves by any

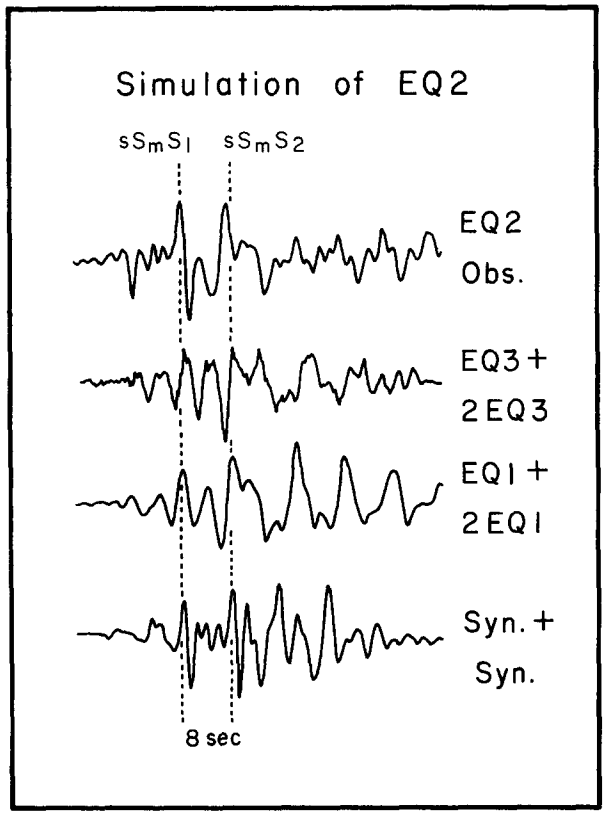

FIG. 13. Attempts to reproduce EQ2 by adding the tangential components of various events together. In all cases an 8 sec delay is used and the second subevent is scaled to be twice as large as the first. The uppermost waveform is EQ2 at PAS; the second is the aftershock EQ3 added to itself; the third is EQ1 added to itself; the fourth is the synthetic for EQ3 added to itself.

of these combinations to the extent observed in EQ2, and this feature remains unexplained.

An 8-sec total delay implies that the subevents occurred close together. The start time separation is 7 ± 0.5 sec. The remaining delay of 1 ± 0.5 sec is due to the travel-time difference. If, as the teleseismic modeling predicts, the second subevent is shallower than the first, then about 0.7 sec of the travel-time difference is taken up by the depth difference and the remainder is due to the horizontal separation of the two subevents. Because PAS is relatively close to the epicenter, the observed record contains only crustal phases. The observed travel-time difference indicates that the source separation is of the order of a few kilometers. Even if we put both subevents at the same depth, we obtain a small source separation.

In summary, we have modeled the Superstition Hills earthquakes both synthetically and by mapping the data of one event into that of the other. EQ1 was a simple pure strike-slip earthquake on a vertical plane striking 45° and exhibiting left-lateral surface rupture. It was a relatively deep event occurring at a depth of 10 km with a teleseismic long-period moment of 2.7×10^{25} dyne cm. EQ2 was a more complex event consisting of—to a first approximation—two subevents similar to EQ1, neglecting the small foreshock. The first subevent occurred at a depth of 10 km and had the following mechanism: $\theta = 35°$, $\delta = 80°$ and $\lambda = 175°$. Its teleseismic moment is 3.6×10^{25}. The second subevent occurred 7 ± 0.5 sec later at a depth of at least 6 km and probably deeper. It had a strike of 320° and the same dip and

rake as subevent 1, and a moment of 7.2×10^{25}. The teleseismic data indicate that subevent 2 occurred 30 km south of subevent 1. The strong-motion data, however, are more compatible with a source separation of only a few kilometers. The uncertainty in the source time separation (±1 sec) at teleseismic distances results in a large uncertainty in the spatial separation (±20 km), so there may not be a conflict between the teleseismic and strong-motion results. Alternatively, the high-frequency strong-motion energy and the long-period energy may have been preferentially produced by different fault segments; that is, the high frequency component is determined by asperities and lower stress drop regions produce the long-period teleseismic results.

ACKNOWLEDGMENTS

Janice Regan and Bob Halliday of the Geological Survey of Canada provided us with the Canadian data. Cindy Arvesen drafted the figures. Art Frankel provided us with an excellent review. California Institute of Technology, Division of Geological and Planetary Sciences contribution no. 4712. This work was supported by USGS Contract 14-08-0001-21912.

REFERENCES

Ben-Menahem, A., S. W. Smith, and T. L. Teng (1965). A procedure for source studies from spectra of long-period seismograms, *Bull. Seism. Soc. Am.* **55,** 203–235.

Frankel, A. and L. Wennerberg (1988). Rupture process of the November 24, 1987 Superstition Hills earthquake determined from strong motion recordings (abstr.), *Seism. Res. Lett.* **59,** 48–49.

Frankel, A. and L. Wennerberg (1989). Rupture process of the M_S 6.6 Superstition Hills earthquake determined from strong-motion recordings: application of tomographic source inversion, *Bull. Seism. Soc. Am.* **79,** 515–541.

Fuis, G. S., W. D. Mooney, J. H. Healey, G. A. McMechan, and W. J. Lutter (1982). Crustal structure of the Imperial Valley region, in *The Imperial Valley, California, earthquake of October 15, 1979, U.S. Geol. Surv. Profess. Paper 1254,* 25–50.

Hartzell, S. and D. V. Helmberger (1982). Strong-motion modeling of the Imperial Valley earthquake of 1979, *Bull. Seism. Soc. Am.* **72,** 571–596.

Ho-Liu, P. and D. V. Helmberger (1989). Modeling regional Love waves: Imperial Valley to Pasadena (submitted for publication).

Jeffreys, H. and K. E. Bullen (1940). *Seismological Tables,* British Association for the Advancement of Science, Gray-Milne Trust.

Langston, C. A. and D. V. Helmberger (1975). A procedure for modelling shallow dislocation sources, *Geophys. J. R. Astr. Soc.* **42,** 117–130.

Magistrale, H., L. Jones, and H. Kanamori (1989). The Superstition Hills, California, Earthquakes of 24 November 1987, *Bull. Seism. Soc. Am.* **79,** 239–251.

Wald, D. J. and P. G. Somerville (1988). Simulation of accelerograms of the 1987 Superstition Hills earthquake sequence, SSA Meeting, May 1988, Honolulu, Hawaii.

Wallace, T. C. and D. V. Helmberger (1982). Determining source parameters of moderate-size earthquakes from regional waveforms, *Phys. Earth Planet. Interiors* **30,** 185–196.

Williams, P. L. and H. W. Magistrale (1989). Slip along the Superstition Hills fault associated with the 24 November 1987 Superstition Hills, California, earthquake, *Bull. Seism. Soc. Am.* **79,** 390–410.

SEISMOLOGICAL LABORATORY
CALIFORNIA INSTITUTE OF TECHNOLOGY
PASADENA, CALIFORNIA 91125

Manuscript received 16 August 1988